

Unveiling the dark Universe with HI and EMBER-2

Mauro Bernardini¹,^{*} Robert Feldmann¹, Daniel Anglés-Alcázar²,[†] Philipp Denzel³, Jindra Gensior⁴

¹*Department of Astrophysics, Universität Zürich, Winterthurerstrasse 190, 8057, Zurich, Switzerland*

²*Department of Physics, University of Connecticut, 196 Auditorium Road, U-3046, Storrs, CT 06269-3046, USA*

³*Centre for Artificial Intelligence, Zurich University of Applied Sciences ZHAW, Technikumstrasse 71, Winterthur 8400, Switzerland*

⁴*Institute for Astronomy, University of Edinburgh, Blackford Hill, Edinburgh, EH9 3HJ, UK*

Accepted XXX. Received YYY; in original form ZZZ

ABSTRACT

Next-generation radio telescopes will provide unprecedented data volumes of the neutral hydrogen (HI) distribution across cosmic time. Combining weak lensing surveys with spatial and kinematic observations of HI could help constrain key properties of dark matter, such as its mass, clustering behavior, and spatial distribution. However, inferring dark matter properties from HI observations is challenging because of processes related to galaxy formation, such as stellar feedback. Methods that use empirical relations, often calibrated via numerical simulations, do not use full field-level information to model the complex relation between dark matter and HI. We address this shortcoming with a data-driven approach, leveraging the recently introduced EMBER-2 model to learn the HI-dark matter mapping at the field level for a wide redshift range, $z = 6 - 0$. After training on cosmological galaxy formation simulations run with FIRE-2, EMBER-2 accurately recovers key statistics, including dark matter mass fractions and surface density profiles. The HI-dark matter density cross-correlation is reconstructed at an accuracy of 10% down to scales of $k = 100 h/c\text{Mpc}$, a significant improvement over traditional approaches. The presented method may become a key ingredient in future inference pipelines as it can be readily integrated into downstream analysis tasks of radio surveys.

Key words: large-scale structure of Universe – dark matter – galaxies: haloes – galaxies: formation – methods: numerical – methods: statistical

1 INTRODUCTION

The next generation of radio and optical surveys will provide an unprecedented volume of data to analyze. Pathfinder surveys such as MeerKAT’s MIGHTEE (Maddox et al. 2021; Jarvis et al. 2025) and ASKAP’s RACS (McConnell et al. 2020; Duchesne et al. 2024; Duchesne et al. 2025), and in the near future the Square Kilometre Array (SKA) telescopes (Weltman et al. 2020), are revolutionizing our ability to probe the distribution and kinematics of HI across a significant fraction of cosmic time. These surveys will provide detailed observations of HI in the Interstellar (ISM) and Circumgalactic Medium (CGM) and map the large-scale structures of the cosmic web with Intensity Mapping (IM) (Paul et al. 2021; Cunnington et al. 2023; Mazumder et al. 2025). Complementary optical and near-infrared facilities such as the Extremely Large Telescope (ELT) and upcoming wide-field surveys from Euclid (Euclid Collaboration et al. 2019, 2024) and the Vera C. Rubin Observatory’s LSST (Sheldon et al. 2023) will provide large galaxy catalogs extending to high redshifts and play a crucial role for weak lensing (WL) studies. In particular, LSST and Euclid will measure cosmic shear across large regions of the sky, allowing precise constraints on the total matter distribution. By combining WL with HI IM, these efforts will offer

a multi-faceted approach to constrain key properties of dark matter, such as its mass, and the processes governing cosmic structure formation (e.g. Abdalla et al. 2015; Pourtsidou et al. 2016; Sangka & Bacon 2024).

However, directly inferring the underlying dark matter distribution from observational data remains challenging. While WL provides a direct probe of the total matter field, it requires large statistical samples (Takada 2014; Pérez de los Heros 2020; Mahony et al. 2022; Remy et al. 2023). Furthermore, measuring the matter power spectrum requires accurate modeling of all systematic effects that contribute to the cosmic shear signal. Of particular importance is the impact of baryonic feedback stemming from small-scale processes that can severely affect the cosmic shear power spectrum on small angular scales (e.g. Mohammed et al. 2014; Schneider & Teyssier 2015; Schneider et al. 2019; Huang et al. 2019; Schneider et al. 2020; Lu & Haiman 2021; Broxterman et al. 2024).

HI based methods offer a complementary approach by modeling HI as a biased tracer of the underlying dark matter field. These approaches establish the mapping between HI and dark matter via empirical relations derived from numerical simulations that are themselves tuned to match key observational constraints, such as the stellar mass function or the power spectrum. For example, Halo Occupation Distribution (HOD) models and abundance matching (AM) techniques construct a mapping between the mass of dark matter haloes and the contained HI mass (e.g. Berlind & Weinberg 2002;

* mauro.bernardini@uzh.ch

† Authors listed in alphabetical order

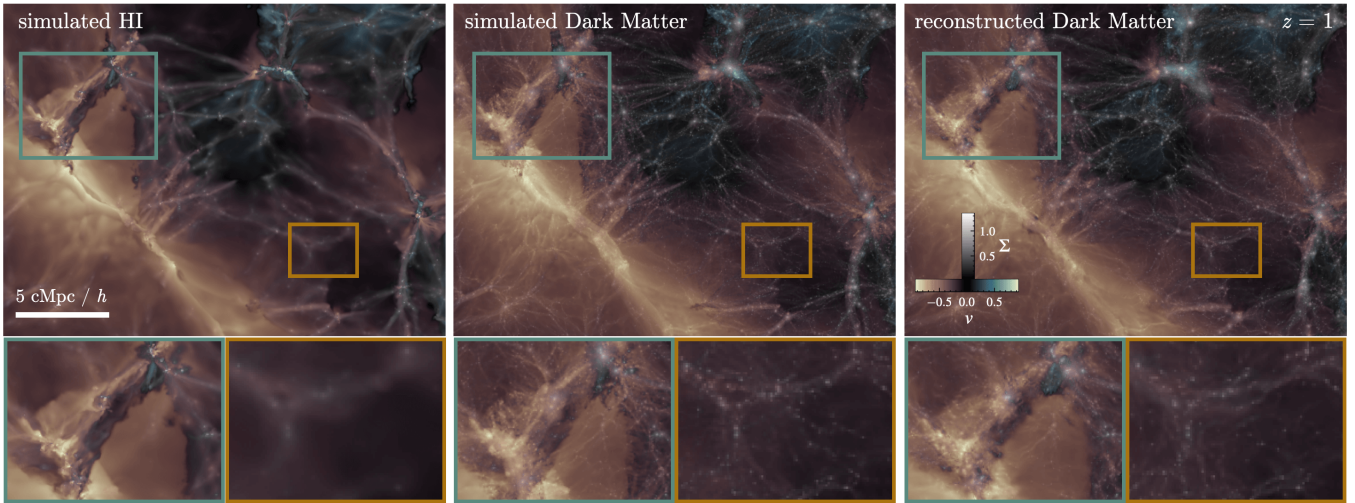


Figure 1. Overview figure showing an example region of the simulated HI and DM fields in the FB30 simulation and the corresponding reconstructed field from EMBER-2 at $z = 1$. The figure shows both normalized channels, surface density Σ and line-of-sight velocity v , in a composite manner, where increased brightness indicates higher Σ , color-coded by the corresponding velocity of each pixel (from red to blue). For better visibility we show the normalized field values, which have $O(1)$. This visual comparison highlights that the HI density and velocity fields contain significant amounts of information across different phase-space regimes, which can be used to accurately reconstruct the underlying DM distribution and kinematics from large down to small scale structures. Shown as insets are two example regions showcasing this behavior in both a high (teal) and low (orange) density regime.

Villaescusa-Navarro et al. 2014; Castorina & Villaescusa-Navarro 2017; Qin et al. 2022). Other methods model the relation as a bias expansion (BE) on the field level, where the HI and dark matter density fields are fitted with analytical descriptions with a few bias parameters (Obuljen et al. 2023; Baradaran et al. 2024; de Belsunce et al. 2025).

However, these approaches do not fully capture the complex interplay between HI and dark matter, especially on small scales, since the relation is established by either considering just a few quantities, such as the halo mass for HOD, or only a handful of fitting parameters in the BE, while discarding the remaining information stored in the field. Furthermore, the correlation between HI and the underlying dark matter distribution is altered by feedback processes, such as stellar winds, ram pressure stripping and feedback from Active Galactic Nuclei (AGN), that redistribute baryonic matter (Anglés-Alcázar et al. 2017; Hafen et al. 2019; Gebhardt et al. 2024). These processes complicate dark matter inference from just a few simple HI properties, since environmental effects play a significant role in driving the scatter in the HI to dark matter halo mass relation. This behavior has been seen in observations (Oosterloo et al. 2010; Janowiecki et al. 2017; Cortese et al. 2021; Li et al. 2022; Saintonge & Catinella 2022; Saraf et al. 2024) and has been successfully reproduced in simulations (e.g. Rafieferantsoa et al. 2015; Stevens et al. 2019; Bernardini et al. 2022).

To address these challenges, we propose a data-driven approach to learn the direct mapping from HI to the underlying dark matter distribution by taking into consideration the entire field level information. By leveraging neural networks trained on cosmological simulations, we construct a model that captures the complex, non-linear relationship between HI and dark matter while accounting for baryonic effects. Unlike statistical techniques that assume a fixed bias relation between baryons and dark matter, this approach allows for a more adaptive and accurate reconstruction of the dark matter field in different cosmic environments, including larger and smaller halos, filaments, and voids. In particular, we leverage the recently introduced

EMBER-2 model (Bernardini et al. 2025) to learn the mapping between HI and dark matter density and kinematic information. We train EMBER-2 on 2-dimensional maps of surface density and radial velocity. Compared to approaches like HOD that produce point estimates, this method also allows to reconstruct dark matter properties derived from the field level, such as e.g. radial profiles of dark matter density. We present a visual summary of this approach in Figure 1 which shows composite images of surface density and radial velocity information for the HI input field and the simulated and reconstructed dark matter fields. Also shown are two inset regions centered on a high and a very low HI density patch to highlight the large dynamic range between different regions in the cosmic web.

This letter is structured in the following way. In section 2 we present the simulations used for the training data. Section 3 briefly introduces the EMBER-2 framework and describes the training of the networks, whereas we discuss the results in section 4 and conclude in section 5.

2 SIMULATIONS

Similar to the approach in Bernardini et al. (2025) we use cosmological hydrodynamical simulations that are part of the Feedback in Realistic Environments (FIRE¹) project. The simulation used to create the training dataset is a volume simulation from the FIREbox suite (Feldmann et al. 2023, 2025) with a box length of 30 cMpc/h (44 cMpc; hereafter denoted as FB30, Bernardini et al. 2025). The simulation is run with GIZMO (Hopkins 2015)² using the FIRE-2 galaxy formation physics model (Hopkins et al. 2018). The initial conditions for the simulation are created using MUSIC (Hahn & Abel 2011).

¹ See the official FIRE project website: fire.northwestern.edu

² A public version of GIZMO is available at tapir.caltech.edu/phopkins/Site/GIZMO

The simulations are run with Planck 2015 cosmology (Planck Collaboration et al. 2016): $H_0 = 67.74$ km/s/Mpc, $\Omega_m = 0.3089$, $\Omega_\Lambda = 0.6911$, $\Omega_b = 0.0486$, $\sigma_8 = 0.8159$ and $n_s = 0.9667$. The FIRE-2 galaxy formation model has been validated both in zoom-in and cosmological box simulations, for large-scale (e.g. Bernardini et al. 2022; Tortora et al. 2024) and small-scale HI properties (e.g. Feldmann et al. 2023; Gensior et al. 2023, 2024). The simulation is initialized with 1024^3 dark matter and 1024^3 gas particles with mass resolutions of $m_{\text{dm}} = 1.45 \times 10^6 M_\odot$ and $m_{\text{gas}} = 5 \times 10^5 M_\odot$. For dark matter (star) particles the softening length is fixed to 160 pc (32 pc). Gas particles have a variable softening lengths with a minimum of 4 pc. The most massive dark matter halo at $z = 0$ has a mass of $2.36 \times 10^{13} M_\odot$, and the resolution of the simulation allows to resolve halos down to $\sim 10^9 M_\odot$ (with $\geq 10^3$ particles). Dark matter halos are identified with the Amiga Halo finder (AHF) (Knollmann & Knebe 2009).³ In addition to FB30, we use the FB512 simulation from the FIREbox simulation suite, hereafter denoted as FB15. This simulation is generated with a different random seed than FB30, but uses the same physics and resolution, albeit in an 8 times smaller volume. In this work, FB15 is only used as an independent test set to verify the models accuracy of the dark matter reconstruction.

3 EMBER-2

EMBER-2 is a neural network based model introduced in Bernardini et al. (2025), designed to perform probabilistic mapping from dark matter to baryon fields across a large range of redshifts ($z = 6 - 0$). In this letter we retrain the EMBER-2 model on the task of reconstructing the underlying dark matter fields from the simulated HI counterparts. The task of our model is to perform the mapping from 2-dimensional projected HI density and radial velocity (x) to 2-dimensional dark matter density and radial velocity (y) for the redshift interval $z = 6 - 0$, i.e. for each redshift the model learns the following probabilistic mapping

$$f : (\Sigma_{\text{HI}}, v_{\text{HI}}) \rightarrow (\Sigma_{\text{dm}}, v_{\text{dm}}). \quad (1)$$

EMBER-2 is a conditional GAN (cGAN) (Goodfellow et al. 2014; Mirza & Osindero 2014) encompassing two neural networks. The training task of the generator G consists of generating dark matter samples, $G(\eta|x, z)$, that are following the true data distribution p_y as closely as possible. Here, η is a noise input drawn from a normal distribution, x the conditional HI map and z the redshift. Given x , the discriminator D is tasked to distinguish between real (y) and generated samples ($G(\eta|x, z)$). In this process G implicitly learns the underlying conditional probability $p(y|x, \eta)$, which is inferred implicitly and thus intractable. The loss functions are designed such that the two networks compete in an adversarial game, trying to outperform their respective opponent. We use the non-saturating GAN losses (Goodfellow et al. 2014),

$$\mathcal{L}_D = -\mathbb{E}_\eta [\ln(1 - D(G(\eta|x, z)|x, z))] - \mathbb{E}_y [\ln D(y|x, z)] \quad (2)$$

$$\mathcal{L}_G = -\mathbb{E}_\eta [\ln D(G(\eta|x, z)|x, z)] \quad (3)$$

where y and x are samples from the true data distributions p_y and p_x . \mathbb{E} is the expectation operator. We follow the same approach as in Bernardini et al. (2025) to produce the datasets for training and testing the neural network model. Briefly, we use equidistant spacing of 0.25 between redshifts $6 \geq z \geq 2$ and a spacing of 0.1 between $2 \geq z \geq 0$. We deposit the particle information aggregated in slabs of

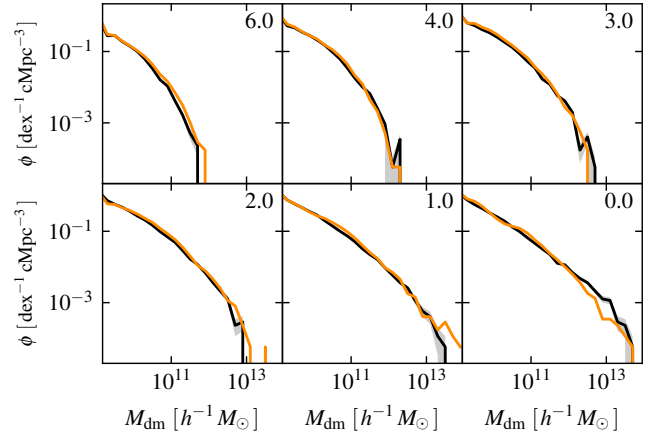


Figure 2. Structure mass function ϕ for the simulated (black) and reconstructed (orange) dark matter maps at different redshifts (indicated in the top right). The shaded bands indicate the 16th to 84th percentile, while the thick line shows the median relation. The mass functions were computed by aggregating all slices in the test dataset into a single mass function, while uncertainties were computed from the different test boxes with varying noise realizations. Only structures with masses above $10^9 h^{-1} M_\odot$ are shown corresponding to structures resolved by at least 10^3 dark matter particles.

$1.5 \text{ Mpc}/h$ for HI and dark matter onto 2-dimensional grids of 1024^2 pixels and a spatial resolution of $\sim 29 \text{ cMpc}/h$ using the smooth and tipgrid codes.⁴ During training we randomly crop patches of 128^2 pixels from the projections and add random rotation and flipping as data augmentation. We use a 3-fold cross-validation approach, where we take the projections from two axes for training while the remaining axis of FB30 is used for testing. Additionally, we complement the testing dataset with all axes from the FB15 simulation.

We make use of the scaling functions introduced in Bernardini et al. (2025) to normalize the HI and dark matter surface density and velocity fields. We emphasize that we do not perform any additional hyper-parameter tuning, but rather use the same parameter setup that was used to train the EMBER-2 model as presented in Bernardini et al. (2025).⁵

4 RESULTS AND DISCUSSION

Figure 1 presents a composite image displaying the two HI input channels (left), the simulated dark matter counterpart (middle), and the reconstructed result (right) for an example region at $z = 1$. The two inset regions (highlighted in teal and orange) illustrate the performance of EMBER-2 across a wide dynamic range of densities and velocities, highlighting structural similarity between the simulation and the emulation.

We evaluate the neural network performance using a variety of summary statistics to probe field-level metrics and quantities derived from individual dark matter structures. Specifically, we analyze halo-based metrics including the halo mass function, mass-size relation of halos, HI fractions and halo profiles. We also perform a cross-correlation analysis to quantify the spectral statistics of the reconstructed fields.

⁴ Code is publicly available on github.com/N-BodyShop.

⁵ For additional details we refer the reader to the official project website maurbe.github.io/ember2.

³ See the official AHF website: popia.ft.uam.es/AHF/.

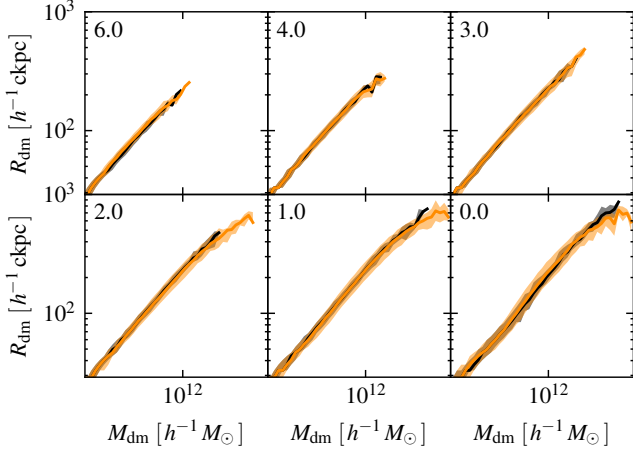


Figure 3. Dark matter structure mass-size relation in the simulation (black) and reconstruction (orange) at different redshifts (indicated in the top left). For both simulation and reconstruction we show the median relation (thick line) as well as the 16th to 84th percentiles region (shaded bands).

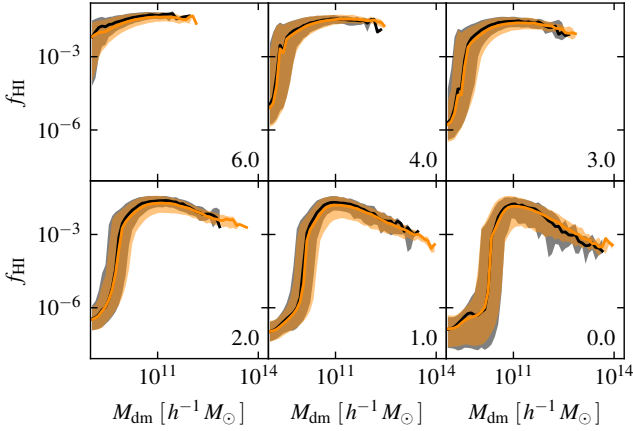


Figure 4. Dark matter structure mass to HI fraction in the simulation (black) and reconstruction (orange) for all tested redshifts. The thick lines and shaded regions show the medians and 16th to 84th percentiles as function of structure mass.

For the simulation, halo catalogs can readily be computed using AHF and are used to compute halo-based metrics. However, we do not have access to such catalogs for the reconstructed maps. Thus, we define the following algorithm to analyze dark matter structures in 2-d maps that can be compared between simulation and emulation:⁶

(i) A threshold is applied to the dark matter density map where only pixels with values $\geq n_\delta \cdot \delta$ are retained, where $\delta = \Sigma_{\text{dm}} / \overline{\Sigma_{\text{dm}}} - 1$. n_δ is a free parameter that we set to 10, such that the abundance of halos at a dark matter mass of $10^{11} h^{-1} M_\odot$ is similar to the AHF result.

(ii) Peaks in the thresholded map are identified using a local maxima finder. These mark the centers of the dark matter structures.

(iii) Using these centers and the thresholded image, we use the watershed segmentation, which "floods" the image from the prede-

⁶ The entire algorithm is implemented using [scikit-image](#).

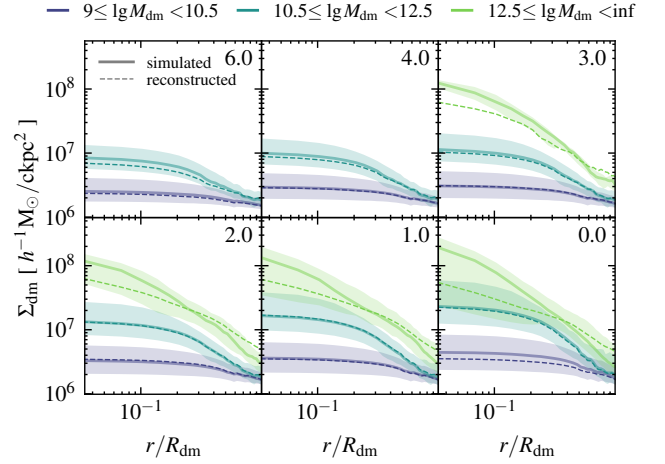


Figure 5. Simulated (solid) and reconstructed (dashed) dark matter surface density profiles as a function of normalized structure radius R_s and redshift (top right). Different colors correspond to varying mass bins, where the largest mass bin only gets populated after $z < 4$ due to the hierarchical growth of structures. Individual lines indicate the median relations whereas shaded regions show the 16th to 84th percentiles for the simulation. For consistent comparison across structure mass bins, radial profiles are interpolated onto a uniform set of r/R_{dm} values using bilinear interpolation.

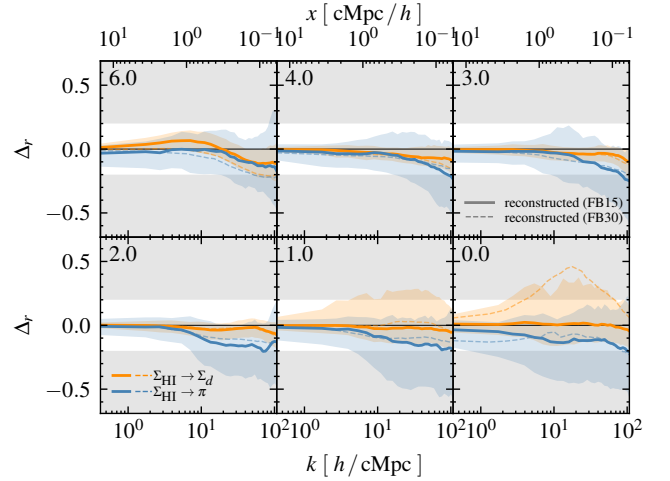


Figure 6. Median errors on the cross-correlation coefficients between the HI and dark matter surface densities Σ_{HI} and Σ_{dm} (orange), as well as for the kinetic energy density surface density π (blue), for all test redshifts. Solid and dashed lines represent the results on the FB15 and the FB30 test set for both Σ_{HI} and π . For FB15 we also show the 16th to 84th percentiles as shaded regions. The white region indicates the 20% error band.

finer centers and assigns connected pixels to their corresponding structures.

(iv) We discard any structure with a total dark matter mass that is $\leq 10^9 h^{-1} M_\odot$ (corresponding to 10^3 particles) to only preserve well-resolved structures.

(v) We assign a size R_{dm} to each structure according to $R_{\text{dm}} = \sqrt{A_{\text{dm}}/\pi}$ where A_{dm} is the structure area. We have checked that identified structures are roughly spherical, and thus the above assumption is suitable for the analysis performed here.

(vi) For each structure we compute its total dark matter mass $M_{\text{dm}} = \Sigma_{\text{dm}} \times A_{\text{dm}}$, as well as its HI fraction f_{HI} defined as the ratio of the HI mass contained in A_{dm} and M_{dm} .⁷ Furthermore, radial profiles $\Sigma_{\text{dm}}(r)$ are extracted by computing the average surface density for concentric annuli around the patch center.

We then apply this algorithm to the simulated and reconstructed dark matter maps and use the resulting structure catalogs in our further analysis.

Mass function, mass-size relation and HI fraction: From the catalogs we compute the structure mass function (SMF) $\phi \equiv dn/d\lg M_{\text{dm}}$, i.e. the number of identified structures as a function of their dark matter mass M_{dm} . We show the result in Figure 2 for selected redshifts $z = 6 - 0$. The comparison between simulated (black) and reconstructed (orange) maps shows that EMBER-2 emulates realistic number statistics of dark matter structures at all redshifts, especially for $\lg M_{\text{dm}} \leq 12$. For more massive systems, the comparison becomes more difficult due to the lower number of present structures, and the statistic is mostly affected by Poisson noise. Figure 3 shows the mass-size relation of identified structures. EMBER-2 shows excellent agreement with the simulation, for $\lg M_{\text{dm}} \leq 13$, while the results suggest that EMBER-2 predicts slightly less compact structures in the very high mass end.

We also show the simulated and reconstructed HI mass fractions, f_{HI} , of structures in Figure 4. The results for f_{HI} as a function of structure mass M_{dm} are excellent over the entire mass range, capturing the very HI deficient small structures, the sharp upturn and peak of f_{HI} , and its subsequent decrease at higher masses for $z \leq 2$. Furthermore, for all redshifts and mass regimes, EMBER-2 also accurately reconstructs the correct intrinsic scatter in f_{HI} over the entire dynamic range.

Radial profiles: We show the dark matter surface density profiles in Figure 5 for three selected mass bins. The reconstructed profiles of structures with $\lg M_{\text{dm}} \leq 12.5$ are in good agreement with the simulation. In fact, EMBER-2 is capable of reconstructing the correct amplitudes and slopes both in the inner and outer part of structures. The largest deviation occurs in the very high mass end, $\lg M_{\text{dm}} \geq 12.5$, where EMBER-2 systematically underestimates the amplitude, approximately by a factor of 2 at $z = 0$, and predicts a too shallow density drop in the outer regions. We attribute this behavior to the small sample size in this mass regime.

Cross-correlations: After $z \lesssim 6$ the HI density distribution increasingly decouples from the underlying dark matter distribution. In fact, for $z \lesssim 2$ almost the entire HI mass resides within dark matter halos (see e.g. Feldmann et al. 2023). Hence, the scale at which the two fields decouple increases for lower redshifts, which is measured by the cross-correlation coefficient (see e.g. Figure 2 in Bernardini et al. 2025). For a specific property φ (e.g. surface density), the cross-correlation coefficient is defined through the power spectra of dark matter ($P_{\text{dm},\varphi}$) and HI ($P_{\text{HI},\varphi}$) and their corresponding cross-power spectrum $P_{\text{dm+HI},\varphi}^{\times}$, as

$$r(k) = \frac{P_{\text{dm+HI},\varphi}^{\times}}{\sqrt{P_{\text{dm},\varphi} P_{\text{HI},\varphi}}}. \quad (4)$$

We define the error on the cross-correlation coefficient as $\Delta_r = \text{median}(r_p/r_y - 1)$. To quantify the correlations between individual

dark matter channels, we also combine the two quantities Σ_{dm} and v_{dm} to derive the kinetic surface energy density, $\pi = \Sigma_{\text{dm}} v_{\text{dm}}^2 / 2$. In Figure 6 we show Δ_r at different redshifts by correlating the input density field Σ_{HI} with Σ_{dm} , as well as Σ_{HI} with π . The results on the FB15 (FB30) test are shown as solid (dashed) lines, while we also show the 16th to 84th percentiles for FB15. The results show that EMBER-2 is capable of reconstructing the correct cross-correlations between those fields with errors less than 10% for Σ_d and 20% for π , for most redshifts and k -scales. This result holds both for the FB15 and FB30 test sets. Traditional HOD (BE) methods typically achieve an accuracy of 10% (50%) for $k \lesssim 1h/\text{Mpc}$ at $z = 0$ (see e.g. Wadekar et al. 2021; Obuljen et al. 2023), highlighting the additional information stored in the field. The only noticeable exception for FB30 occurs at $z = 0$ where Δ_r between Σ_{HI} and Σ_{dm} is raised to $\sim 50\%$. We have investigated this behavior and found that it originates in the small number of massive halos in FB30, while Δ_r is disproportionately sensitive to the highest mass systems for large values of k (see Figure 10 in Bernardini et al. 2025). In fact, for FB15 the model reconstructs the cross-correlation coefficients with deviations of maximum $\sim 10\%$ for the surface density and $\sim 20\%$ for the radial velocity fields for all k -scales, motivating the conclusion that the deviation in FB30 is due to the small sample size of massive systems.

5 SUMMARY AND OUTLOOK

In this letter we have used the EMBER-2 framework to learn the mapping between HI and dark matter on the field level over the redshift range $z = 6 - 0$. Our analysis demonstrates that EMBER-2 can accurately reconstruct dark matter density and velocity fields from HI observations, with the correct number statistics, mass-size relations and HI fractions over a wide range of masses. Furthermore, it successfully captures both the large-scale correlations and internal density distributions of structures, and accurately reconstructs the radial density profiles of structures with $\lg M_{\text{dm}} \lesssim 12.5$. Additionally, the cross-correlation analysis shows good agreement between predicted and true dark matter density and kinematics, with maximum deviations of 10% and 20% respectively, up to scales of $k = 100 h/c\text{Mpc}$.

In the following we highlight the impact of the method for upcoming HI surveys and dark matter inference studies:

- Given the fully convolutional architecture of EMBER-2, the method can be used for both large- and small scale dark matter inference, since it captures the correct correlations between HI and dark matter on Mpc scales, as well as accurately reconstructs the density profiles of halos on small scales. Thus, this framework can be adaptively tuned to both large scale HI observations such as HI IM as well as small scale observations probing the HI field within individual halos.

- Our method naturally allows to incorporate simulations with multiple stellar and AGN feedback models. This will improve the methods's generalizability across different astrophysics models to marginalize over baryonic effects, which is of particular importance to WL studies. Since individual maps can be sampled on time-scales of \sim seconds, the presented method is fast enough to be incorporated in downstream analysis pipelines with realistic observations.

- To adapt to observational limitations, future iterations may also train on degraded HI maps to match sensitivity limits of the SKA telescopes at different redshifts. In this pipeline the simulated HI fields are first degraded according to expected observational noise

⁷ Unless otherwise stated, masses are in units of M_{\odot} .

levels and resolutions, and subsequently used as input for EMBER-2 to reconstruct the underlying dark matter distribution. This extended framework is well-suited for existing and developing analysis frameworks, such as KARABO⁸ (Sharma et al. 2025), with its submodules OSKAR and RASCIL for simulating instrumental systematics and noise contamination. This integration may enable joint modeling between simulated and observational data facilitating parameter inference in realistic observational scenarios.

• Finally, expanding the input feature space of EMBER-2 in principle straight-forward, and thus, additional channels, such as the stellar light measured from upcoming optical surveys (e.g. LSST, ELT) may be readily integrated. This multi-wavelength approach could likely enhance the accuracy of dark matter reconstructions by leveraging observational tracers complementary to HI.

These additions may broaden the applicability of the EMBER-2 framework to a wider range of physical models (e.g. Villaescusa-Navarro et al. 2021; Rose et al. 2025), while also incorporating observational effects. Paired with HI observations, such a model could readily be used together with sampling algorithms to perform parameter inference to constrain the physics of dark matter while marginalizing over baryonic effects.

ACKNOWLEDGMENTS

The FB15 simulation was supported in part by computing allocations at the Swiss National Supercomputing Centre (CSCS) under project IDs s697, s698, and uzh18. The FB30 simulation was supported by computing allocations at CSCS under project IDs s1255 and uzh18. MB and RF acknowledge financial support from the Swiss National Science Foundation (grant no 200021_188552 and CRSII5_193826). DAA acknowledges support from NSF CAREER award AST-2442788, NASA grant ATP23-0156, STScI grants JWST-GO-01712.009-A, JWST-AR-04357.001-A, and JWST-AR-05366.005-A, an Alfred P. Sloan Research Fellowship, and Cottrell Scholar Award CS-CSA-2023-028 by the Research Corporation for Science Advancement. This work made use of infrastructure services provided by S3IT, the Service and Support for Science IT team at the University of Zurich. The following software was used in this work: Numpy (Harris et al. 2020), Matplotlib (Hunter 2007), scikit-learn (Pedregosa et al. 2011) and PyTorch (Paszke et al. 2019).

DATA AVAILABILITY STATEMENT

The data used to produce the plots will be made available upon reasonable request to the corresponding author.

REFERENCES

Abdalla F. B., et al., 2015, in *Advancing Astrophysics with the Square Kilometre Array (AASKA14)*. p. 17 ([arXiv:1501.04035](https://arxiv.org/abs/1501.04035)), [doi:10.22323/1.215.0017](https://doi.org/10.22323/1.215.0017)
 Anglés-Alcázar D., Faucher-Giguère C.-A., Kereš D., Hopkins P. F., Quataert E., Murray N., 2017, *MNRAS*, **470**, 4698
 Baradaran D., Hadzhiyska B., White M., Sailer N., 2024, *Phys. Rev. D*, **110**, 103517
 Berlind A. A., Weinberg D. H., 2002, *ApJ*, **575**, 587

Bernardini M., Feldmann R., Anglés-Alcázar D., Boylan-Kolchin M., Bullock J., Mayer L., Stadel J., 2022, *MNRAS*, **509**, 1323
 Bernardini M., et al., 2025, *MNRAS*, **538**, 1201
 Broxterman J. C., et al., 2024, *MNRAS*, **529**, 2309
 Castorina E., Villaescusa-Navarro F., 2017, *MNRAS*, **471**, 1788
 Cortese L., Catinella B., Smith R., 2021, *Publ. Astron. Soc. Australia*, **38**, e035
 Cunningham S., et al., 2023, *MNRAS*, **518**, 6262
 Duchesne S. W., et al., 2024, *Publ. Astron. Soc. Australia*, **41**, e003
 Duchesne S. W., et al., 2025, The Rapid ASKAP Continuum Survey (RACS) VI: The RACS-high 1655.5 MHz images and catalogue ([arXiv:2501.04978](https://arxiv.org/abs/2501.04978))
 Euclid Collaboration et al., 2019, *A&A*, **627**, A59
 Euclid Collaboration et al., 2024, *A&A*, **681**, A67
 Feldmann R., et al., 2023, *MNRAS*, **522**, 3831
 Feldmann R., et al., 2025, *MNRAS*, **536**, 988
 Gebhardt M., et al., 2024, *MNRAS*, **529**, 4896
 Gensior J., Feldmann R., Mayer L., Wetzel A., Hopkins P. F., Faucher-Giguère C.-A., 2023, *MNRAS*, **518**, L63
 Gensior J., et al., 2024, *MNRAS*,
 Goodfellow I. J., Pouget-Abadie J., Mirza M., Xu B., Warde-Farley D., Ozair S., Courville A., Bengio Y., 2014, *Generative Adversarial Networks* ([arXiv:1406.2661](https://arxiv.org/abs/1406.2661))
 Hafen Z., et al., 2019, *MNRAS*, **488**, 1248
 Hahn O., Abel T., 2011, *MNRAS*, **415**, 2101–2121
 Harris C. R., et al., 2020, *Nature*, **585**, 357
 Hopkins P. F., 2015, *MNRAS*, **450**, 53
 Hopkins P. F., et al., 2018, *MNRAS*, **480**, 800–863
 Huang H.-J., Eifler T., Mandelbaum R., Dodelson S., 2019, *MNRAS*, **488**, 1652
 Hunter J. D., 2007, *Computing in science & engineering*, **9**, 90
 Janowiecki S., Catinella B., Cortese L., Saintonge A., Brown T., Wang J., 2017, *MNRAS*, **466**, 4795
 Jarvis M. J., et al., 2025, *arXiv e-prints*, p. [arXiv:2506.11935](https://arxiv.org/abs/2506.11935)
 Knollmann S. R., Knebe A., 2009, *ApJS*, **182**, 608
 Li X., Li C., Mo H. J., Xiao T., Wang J., 2022, *ApJ*, **941**, 48
 Lu T., Haiman Z., 2021, *MNRAS*, **506**, 3406
 Maddox N., et al., 2021, *AAP*, **646**
 Mahony C., et al., 2022, *MNRAS*, **513**, 1210
 Mazumder A., et al., 2025, HI Intensity Mapping with the MIGHTEE Survey: First Results of the HI Power Spectrum ([arXiv:2501.17564](https://arxiv.org/abs/2501.17564))
 McConnell D., et al., 2020, *Publ. Astron. Soc. Austral.*, **37**, e048
 Mirza M., Osindero S., 2014, *Conditional Generative Adversarial Nets* ([arXiv:1411.1784](https://arxiv.org/abs/1411.1784))
 Mohammed I., Martizzi D., Teyssier R., Amara A., 2014, Baryonic effects on weak-lensing two-point statistics and its cosmological implications ([arXiv:1410.6826](https://arxiv.org/abs/1410.6826))
 Obuljen A., Simonović M., Schneider A., Feldmann R., 2023, *Phys. Rev. D*, **108**, 083528
 Oosterloo T., et al., 2010, *MNRAS*, **409**, 500
 Paszke A., et al., 2019, *arXiv e-prints*, p. [arXiv:1912.01703](https://arxiv.org/abs/1912.01703)
 Paul S., Santos M. G., Townsend J., Jarvis M. J., Maddox N., Collier J. D., Frank B. S., Taylor R., 2021, *MNRAS*, **505**, 2039
 Pedregosa F., et al., 2011, *Journal of Machine Learning Research*, **12**, 2825
 Pérez de los Heros C., 2020, *Symmetry*, **12**, 1648
 Planck Collaboration et al., 2016, *A&A*, **594**, A13
 Poursidou A., Bacon D., Crittenden R., Metcalf R. B., 2016, *MNRAS*, **459**, 863
 Qin F., Howlett C., Stevens A. R. H., Parkinson D., 2022, *ApJ*, **937**, 113
 Rafieferantsoa M., Davé R., Anglés-Alcázar D., Katz N., Kollmeier J. A., Oppenheimer B. D., 2015, *MNRAS*, **453**, 3980
 Remy B., Lanusse F., Jeffrey N., Liu J., Starck J. L., Osato K., Schrabback T., 2023, *A&A*, **672**, A51
 Rose J. C., et al., 2025, *ApJ*, **982**, 68
 Saintonge A., Catinella B., 2022, *ARA&A*, **60**, 319
 Sangka A., Bacon D., 2024, *MNRAS*, **532**, 996
 Saraf M., Cortese L., Wong O. I., Catinella B., Janowiecki S., Hardwick J. A., 2024, *MNRAS*, **530**, 2420

⁸ Code website can be found here: github.io/Karabo-Pipeline

- Schneider A., Teyssier R., 2015, *J. Cosmology Astropart. Phys.*, 2015, 049
- Schneider A., Teyssier R., Stadel J., Chisari N. E., Brun A. M. L., Amara A., Refregier A., 2019, *Journal of Cosmology and Astroparticle Physics*, 2019, 020–020
- Schneider A., et al., 2020, *J. Cosmology Astropart. Phys.*, 2020, 020
- Sharma R., et al., 2025, *arXiv e-prints*, p. [arXiv:2504.00303](https://arxiv.org/abs/2504.00303)
- Sheldon E. S., Becker M. R., Jarvis M., Armstrong R., LSST Dark Energy Science Collaboration 2023, *The Open Journal of Astrophysics*, 6, 17
- Stevens A. R. H., et al., 2019, *MNRAS*, 483, 5334
- Takada M., 2014, *IAU Symp.*, 306, 78
- Tortora L., Feldmann R., Bernardini M., Faucher-Giguère C.-A., 2024, *MNRAS*, 532, 3847
- Villaescusa-Navarro F., Viel M., Datta K. K., Choudhury T. R., 2014, *J. Cosmology Astropart. Phys.*, 2014, 050
- Villaescusa-Navarro F., et al., 2021, *ApJ*, 915, 71
- Wadkar D., Villaescusa-Navarro F., Ho S., Perreault-Levasseur L., 2021, *ApJ*, 916, 42
- Weltman A., et al., 2020, *Publ. Astron. Soc. Australia*, 37, e002
- de Belsunce R., Ivanov M. M., Sullivan J. M., Akitsu K., Chen S.-F., 2025, Modeling the Cosmological Lyman- α Forest at the Field Level ([arXiv:2507.00284](https://arxiv.org/abs/2507.00284)), <https://arxiv.org/abs/2507.00284>